

Chapter 3

Designing OFDM Radar Waveform for Target Detection Using Multi-objective Optimization

Satyabrata Sen, Gongguo Tang, and Arye Nehorai

Abstract We propose a multi-objective optimization (MOO) technique to design an orthogonal frequency division multiplexing (OFDM) radar signal for detecting a moving target in the presence of multipath reflections. We employ an OFDM signal to increase the frequency diversity of the system, as different scattering centers of a target resonate variably at different frequencies. Moreover, the multipath propagation increases the spatial diversity by providing extra “looks” at the target. First, we develop a parametric OFDM measurement model for a particular range cell under test, and convert it to an equivalent sparse-model by considering the target returns over all the possible signal paths and target velocities. Then, we propose a constrained MOO problem to design the spectral-parameters of the transmitting OFDM waveform by simultaneously optimizing three objective functions: maximizing the Mahalanobis distance to improve the detection performance, minimizing the weighted trace of the Cramér–Rao bound matrix for the unknown parameters to increase the estimation accuracy, and minimizing the upper bound on the sparse-recovery error to improve the performance of the equivalent sparse-estimation approach.

S. Sen (✉)

Computer Science and Mathematics Division, Oak Ridge National Laboratory, 1 Bethel Valley Road, Oak Ridge, TN 37931, USA
e-mail: sens@ornl.gov

G. Tang

Department of Electrical and Computer Engineering, University of Wisconsin-Madison, 1415 Engineering Drive, Madison, WI 53706, USA
e-mail: gtang5@wisc.edu

A. Nehorai

Preston M. Green Department of Electrical & Systems Engineering, Washington University in St. Louis, 1 Brookings Drive, Saint Louis, MO 63130, USA
e-mail: nehorai@ese.wustl.edu

3.1 Introduction

The problem of adaptive waveform design is becoming increasingly relevant and challenging to modern state-of-the-art radar systems. For many years, conventional radars have transmitted a fixed waveform on every pulse, and the research efforts have been primarily devoted to optimally process the corresponding received signals [50]. However, with the recent technological advancements in the fields of flexible waveform generators and high-speed signal processing hardware, it is now possible to generate and transmit sophisticated radar waveforms that are dynamically adapted to the sensing environments on a periodic basis (potentially on a pulse-by-pulse basis) [7, 23, 35, 55, 56]. Such adaptation can lead to a significant performance gain over the classical (non-adaptive) radar waveforms, particularly in the defense applications involving fast-changing scenarios.

A comprehensive survey on different waveform-design techniques can be found in [38, Chap. 1.2] and references therein; here we briefly discuss some of the salient research work on this topic. Earlier attempts of radar waveform design were to compute parameters of the radar waveform (amplitude, phase, etc.) and the associated receiver response in order to improve the target-detection performance in the presence of clutter and interference [19, 42, 43, 51, 53]. The target-matched illumination techniques are proposed in [22, 25, 41] to optimally design the combination of transmit-waveform and receive-filter for the identification and characterization of targets with known responses. In [5, 29, 44], the information-theoretic optimization criteria, based on the mutual information between the transmit/receive waveform and target response, are considered to design the optimal waveforms for detection, estimation, and tracking problems. Several waveform-optimization algorithms based on the properties of the Cramér–Rao bound (CRB) matrix are presented in [24, 31, 49] for the purpose of target-tracking and parameter estimation. Recently, various constrained waveform-design methodologies are studied to obtain more practical radar waveforms, such as constraining the optimal waveform to have a constant modulus [39], to have a bounded peak-to-average power ratio [14], and to be *similar* to another waveform that has the desired autocorrelation function or ambiguity profile [12, 13, 30, 40].

The waveform-design problems become further intriguing when one needs to simultaneously satisfy two or more optimality criteria, particularly in a multi-mission radar system [4, 21]. Often, the desirable optimization functions are very different and even conflicting to each other, which give rise to dissimilar parameter values for the optimal waveform. To tackle this quandary, the multi-objective optimization (MOO) procedures are employed that concurrently optimize the various objective functions in a Pareto-sense [1, 2, 15, 16, 48]. This type of optimality was originally introduced by Francis Ysidro Edgeworth in 1881 [20] and later generalized by Vilfredo Pareto in 1896 [37].

In this work (see also [47, 48]), we consider a Pareto-optimal waveform-design approach for an orthogonal frequency division multiplexing (OFDM) radar signal to detect a moving target in the presence of multipath reflections, which exist, for example, in urban environments as shown in Fig. 3.1. In [45, 46], we showed that

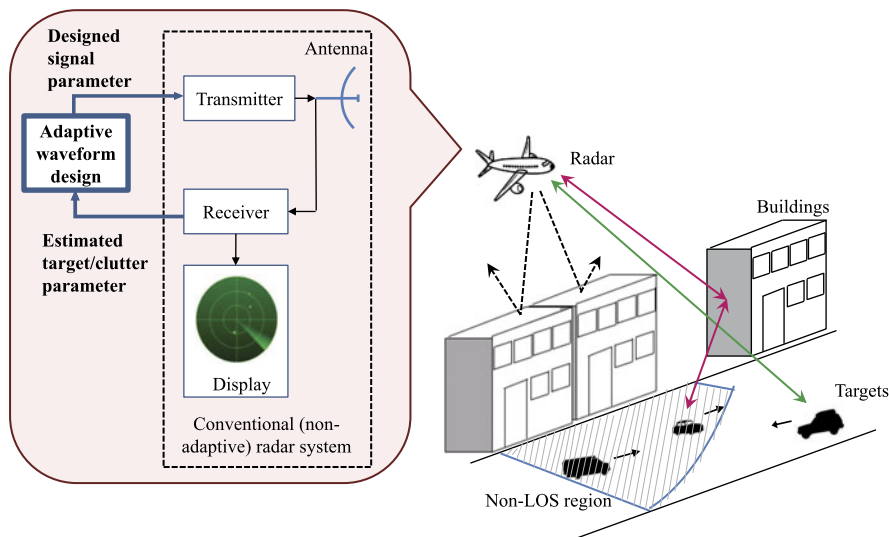


Fig. 3.1 Principle of adaptive waveform design in a radar operating in the multipath scenarios

the target-detection capability can be significantly improved by exploiting multiple Doppler shifts corresponding to the projections of the target velocity on each of the multipath components. Furthermore, the multipath propagations increase the spatial diversity of the radar system by providing extra “looks” at the target and thus enabling target detection and tracking even beyond the line-of-sight (LOS) [28]. To resolve and exploit the multipath components it is common to use short pulse, multi-carrier wideband radar signals. We consider OFDM signaling scheme [34, 36], which is one way to use several subcarriers simultaneously. The use of an OFDM signal mitigates possible fading, resolves multipath reflections, and provides additional frequency diversity as different scattering centers of a target resonate at different frequencies [27, 54].

First, we develop a parametric OFDM measurement model for a particular range cell, to detect a far-field target moving in a multipath-rich environment. We assume that the radar has the complete knowledge of the first-order (or single bounce) specularly reflected multipath signals. Using such knowledge of the geometry, we can determine all the possible paths, be they LOS or reflected, from the range cell under test. However, in practice the target responses reach the radar only via a limited number of paths depending on the position of the target within the range cell. Therefore, considering all the possible signal paths and target velocities, which represent themselves as varying Doppler shifts at the radar receiver, we convert the OFDM measurement model to an equivalent sparse model. The nonzero components of the sparse vector in this model correspond to the scattering coefficients of the target at the true signal paths and target velocity.

The formulation of a sparse-measurement model transforms a target-detection problem into a task of estimating the nonzero coefficients of a sparse signal. To

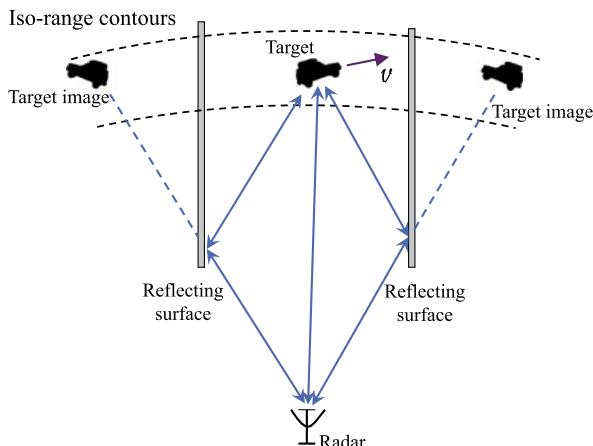
estimate the sparse vector, we propose a sparse-recovery algorithm based on the Dantzig selector (DS) approach [8]. The DS approach belongs to the class of convex relaxation methods in which the ℓ_0 norm is replaced by the ℓ_1 norm that remains a measure of sparsity while being a convex function. However, instead of using the standard DS, in this work we employ a collection of multiple small DS that exploits more prior structures of the sparse vector and provides improved performances both in terms of computational-time and estimation-accuracy [48].

Next, we propose to optimally design the spectral-parameters of the transmitting OFDM waveform for the next coherent processing interval in order to improve the system performance. We formulate and solve a constrained MOO problem [11, 17, 33, 57] that simultaneously optimizes three objective functions. The maximization of the Mahalanobis distance [3, 32] is considered as the first of the three objective functions. This is because the Mahalanobis distance provides a standard measure to quantify the distance between two distributions associated with two hypotheses of a detection problem. However, to compute the Mahalanobis distance in practice, we need to estimate the target scattering-coefficients, velocity, and noise covariance matrix. We characterize the accuracy of such estimations by calculating the CRBs for the unknown parameters, because CRB is a universal lower bound on the variance of all unbiased estimators of a set of parameters [26, Chap. 3]. Therefore, our second objective function tries to minimize a weighted trace of the resultant CRB matrix. Additionally, if we solve the equivalent sparse-estimation problem, then we analyze the reconstruction-performance by evaluating an upper bound on the sparse-estimation error in terms of the ℓ_1 -constrained minimal singular value (ℓ_1 -CMSV) of the sparse-measurement matrix [52]. Compared with the traditional restricted isometry constant (RIC) [9, 10], which is extremely difficult to compute for an arbitrarily given matrix, the ℓ_1 -CMSV is an easily computable measure and provides more intuition on the stability of sparse-signal recovery. Hence, as the third objective function, we propose to minimize the upper bound on the sparse-estimation error for improving the performance of sparse-recovery.

To solve the MOO problem, we apply the well-known nondominated sorting genetic algorithm II (NSGA-II) [18], which belongs to the class of evolutionary algorithms (EAs) and provides a set of solutions known as Pareto-optimal solutions [17]. All the solutions residing on the Pareto-front are considered to be superior to any other solution in the search space when all objectives are considered. The idea of finding as many Pareto-optimal solutions as possible motivates the use of EAs that generate several solutions in a single run. Alternatively, we avoid using the scalarization technique, that transforms a MOO problem into a single-objective one by pre-multiplying each objective with a scalar weight (as done in [15, 16]), primarily for two reasons [17, Chaps. 2, 3]: (i) the optimal solution of a scalarization technique can be very subjective in nature, as it is heavily sensitive to the pre-defined scalar weights used in forming the single-objective function; and (ii) all the Pareto-optimal solutions may not be found by a scalarization approach for the nonlinear and nonconvex optimization problems.

We demonstrate the performance improvement due to the adaptive OFDM-waveform design with several numerical examples. We observe that the Pareto-optimal solutions provide a set of compromised solutions that varies in between

Fig. 3.2 A schematic representation of the multipath scenario



two extrema that are approximately equal to the individual solutions of the objective functions when solved separately. We found that all the Pareto-optimal solutions produce better performances than the fixed waveform, in terms of the Mahalanobis distance and weighted trace of CRB matrix; whereas only a smaller set of the Pareto-optimal solutions has improved performance with respect to the upper bound on sparse-error. Assuming that the noise powers over different subcarriers are the same, we infer that the solution of the Pareto-optimal design redistributes the energy of the transmitted signal by putting the most energy to that particular subcarrier along which the signal-to-noise ratio is the strongest.

The rest of the chapter is organized as follows. In Sect. 3.2, we first develop a parametric OFDM measurement model by incorporating the effects of first-order multipath reflections. Then, in Sect. 3.3, we convert the detection problem to one of sparse-estimation and present a decomposed DS-based sparse-recovery algorithm. In Sect. 3.4, we propose the adaptive OFDM-waveform design algorithm based on the MOO approach. Numerical examples and conclusions are presented in Sects. 3.5 and 3.6, respectively.

3.2 Problem Description and Modeling

Figure 3.2 presents a schematic representation of the problem scenario. We consider a far-field target in a multipath-rich environment, moving with a constant relative velocity \mathbf{v} with respect to the radar. At the operating frequency, we assume that the reflecting surfaces produce only specular reflections of the radar signal, and for simplicity we consider only the first-order reflections. We further assume that the radar has complete knowledge of the environment under surveillance because nowadays accurate information about the city and building layouts can be obtained from lidar imaging systems, blueprints at the city hall, and even public tools such as Google

Maps. Hence, for a particular range cell (the region within the two successive iso-range contours of Fig. 3.2) the radar knows the specific paths, through which the target information reaches the radar receiver, in terms of its direction-of-arrival (DOA) unit-vectors (\mathbf{u}_p , $p = 1, 2, \dots, P$). Under this scenario, our goal here is to decide whether a target is present or not in the range cell under test.

In the following, we first develop a parametric OFDM-measurement model that includes the effects of multipath reflections in between the radar and target. Then, we discuss our statistical assumptions on the clutter and noise.

3.2.1 OFDM Signal Model

We consider a wideband OFDM signaling system with L active subcarriers, a bandwidth of B Hz, and pulse width of T_p seconds. Let $\mathbf{a} = [a_0, a_1, \dots, a_{L-1}]^T$ represent the complex weights transmitted over the L subcarriers, and satisfy $\sum_{l=0}^{L-1} |a_l|^2 = 1$. Then, the complex envelope of the transmitted signal in a single pulse can be represented as

$$s(t) = \sum_{l=0}^{L-1} a_l e^{j2\pi l \Delta f t}, \quad \text{for } 0 \leq t \leq T_p, \quad (3.1)$$

where the subcarrier spacing is denoted by $\Delta f = B/(L + 1) = 1/T_p$. Let f_c be the carrier frequency of operation; then a coherent burst of N transmitted pulses is given by

$$\tilde{s}(t) = 2 \operatorname{Re} \left\{ \sum_{n=0}^{N-1} s(t - nT) e^{j2\pi f_c t} \right\}, \quad (3.2)$$

where T is the pulse repetition interval (PRI). We point out here that in Sect. 3.4 while designing the adaptive waveform we choose the spectral-parameters of the OFDM waveform, a_l s, in order to improve the system performance.

3.2.2 Measurement Model

For a single-pulse, single-carrier transmitted signal $\tilde{s}_l(t) = 2 \operatorname{Re}\{a_l e^{j2\pi f_l t}\}$, where $f_l = f_c + l\Delta f$ is the l th subcarrier frequency, the received signal along the p th path (represented by the DOA unit-vector \mathbf{u}_p) and at the same carrier-frequency f_l can be written as

$$\tilde{y}_{lp}(t) = x_{lp} \tilde{s}_l(\gamma_p(t - \tau_p)) + \tilde{e}_{lp}(t), \quad (3.3)$$

where x_{lp} is a complex quantity representing the scattering coefficient of the target along the l th subchannel and p th path; $\gamma_p = 1 + \beta_p$ where $\beta_p = 2\langle \mathbf{v}, \mathbf{u}_p \rangle / c$ is the

relative Doppler shift along the p th path and c is the speed of propagation; τ_p is the roundtrip delay between the radar and target along the p th path; \tilde{e}_{lp} represents the clutter and measurement noise along the l th subcarrier and p th path. Therefore, the received signal over all P paths due to an L -carrier OFDM signal is given by

$$\begin{aligned}\tilde{y}(t) &= \sum_{l=0}^{L-1} \sum_{p=1}^P \tilde{y}_{lp}(t) = 2 \operatorname{Re} \left\{ \sum_{l=0}^{L-1} \sum_{p=1}^P a_l x_{lp} e^{j2\pi f_l \gamma_p (t - \tau_p)} \right\} + \tilde{e}(t), \\ &= 2 \operatorname{Re} \left\{ \sum_{l=0}^{L-1} \sum_{p=1}^P a_l x_{lp} e^{-j2\pi f_l \gamma_p \tau_p} e^{j2\pi f_l \beta_p t} e^{j2\pi f_l t} \right\} + \tilde{e}(t),\end{aligned}\quad (3.4)$$

and hence the corresponding complex envelope at the output of the l th subchannel is

$$y_l(t) = \sum_{p=1}^P a_l x_{lp} e^{-j2\pi f_l \gamma_p \tau_p} e^{j2\pi f_l \beta_p t} + e_l(t). \quad (3.5)$$

Next, we assume that the relative time gaps between any two multipath signals are very small in comparison to the actual roundtrip delays, i.e., $\tau_p \approx \tau_0$ for $p = 1, 2, \dots, P$. This assumption holds true when the path lengths of multipath arrivals differ little (e.g., in a narrow urban canyon where the down-range is much greater than the width). Further, we consider that the temporal measurements from a specific range gate (denoted by the roundtrip delay τ_0) are collected at every $t = \tau_0 + nT$ instants. Therefore, corresponding to a specific range cell containing the target, the complex envelope of the received signal at the output of the l th subchannel is

$$y_l(n) = \sum_{p=1}^P a_l x_{lp} e^{-j2\pi f_l \gamma_p \tau_0} e^{j2\pi f_l \beta_p (\tau_0 + nT)} + e_l(n). \quad (3.6)$$

Defining

$$\phi_{lp}(n) \triangleq e^{-j2\pi f_l \tau_0} e^{j2\pi f_l \beta_p nT}, \quad (3.7)$$

we can rewrite (3.6) as

$$y_l(n) = a_l \boldsymbol{\phi}_l(n)^T \mathbf{x}_l + e_l(n), \quad (3.8)$$

where $\boldsymbol{\phi}_l(n) = [\phi_{l1}(n), \phi_{l2}(n), \dots, \phi_{lP}(n)]^T$ and $\mathbf{x}_l = [x_{l1}, x_{l2}, \dots, x_{lP}]^T$ are two $P \times 1$ vectors respectively containing the Doppler information and the scattering coefficients of the target at the l th subchannel over all P multipath.

Then, stacking the measurements of all L subchannels into one column vector of dimension $L \times 1$, we get

$$\mathbf{y}(n) = \mathbf{A} \boldsymbol{\Phi}(n) \mathbf{x} + \mathbf{e}(n), \quad (3.9)$$

where

- $\mathbf{y}(n) = [y_0(n), y_1(n), \dots, y_{L-1}(n)]^T$;
- $\mathbf{A} = \text{diag}(\mathbf{a})$ is an $L \times L$ complex diagonal matrix that contains the transmitted weights \mathbf{a} ;
- $\Phi(n) = \text{blkdiag}(\phi_0(n)^T, \phi_1(n)^T, \dots, \phi_{L-1}(n)^T)$ is an $L \times LP$ complex rectangular block-diagonal matrix;
- $\mathbf{x} = [\mathbf{x}_0^T, \mathbf{x}_1^T, \dots, \mathbf{x}_{L-1}^T]^T$ is an $LP \times 1$ complex vector;
- $\mathbf{e}(n) = [e_0(n), e_1(n), \dots, e_{L-1}(n)]^T$ is an $L \times 1$ vector of clutter returns, measurement noise, and co-channel interference.

Finally, concatenating all the temporal data columnwise into an $LN \times 1$ vector, we obtain the OFDM-measurement model as follows:

$$\mathbf{y} = \Psi \mathbf{x} + \mathbf{e}, \quad (3.10)$$

where

- $\mathbf{y} = [\mathbf{y}(0)^T, \mathbf{y}(1)^T, \dots, \mathbf{y}(N-1)^T]^T$;
- $\Psi = [(\mathbf{A}\Phi(0))^T \dots (\mathbf{A}\Phi(N-1))^T]^T$ is an $LN \times LP$ matrix containing the Doppler information of the target;
- $\mathbf{e} = [\mathbf{e}(0)^T, \mathbf{e}(1)^T, \dots, \mathbf{e}(N-1)^T]^T$ is an $LN \times 1$ vector comprising clutter returns, noise, and interference.

3.2.3 Statistical Assumptions

In our problem, the clutter could be the contribution of undesired reflections from the environment surrounding or behind the target, or random multipath reflections from the irregularities on the reflecting surface (e.g., windows and balconies of the buildings in an urban scenario), that cannot be modeled as specular components. In (3.9), the noise vector $\mathbf{e}(n)$ models the clutter returns, measurement noise, and co-channel interference at the output of L subchannels. We assume that $\mathbf{e}(n)$ is a temporally white and circularly symmetric zero-mean complex Gaussian vector, correlated between different subchannels with positive definite covariance matrix Σ . This assumption implies that the OFDM measurements in (3.10) are distributed as

$$\mathbf{y} \sim \mathbb{C}\mathcal{N}_{LN}(\Psi \mathbf{x}, \mathbf{I}_N \otimes \Sigma). \quad (3.11)$$

3.3 Sparse-Estimation Approach

In this section, we reformulate the detection problem of the previous section to a sparsity-based estimation task. Using our knowledge of the geometry, we can determine all the possible signal paths in between the radar and the range cell under test, and subsequently can understand the possible extent of the Doppler variations at the radar receiver. In general, depending on the problem-scenario and target-velocity, a

set of such Doppler shifts could be very large. However, restricting our operation to a narrow region of interest (e.g., an urban canyon where the range is much greater than the width) and a few classes of targets that have comparable velocities (e.g., cars/trucks within a city environment), we can limit the extent of viable Doppler shifts to a smaller quantity.

In the following, we first convert the OFDM-measurement model of (3.10) to a sparse model that accounts for a set of finely discretized Doppler shifts. Then, we present an efficient sparse-recovery approach that employs a collection of multiple small DS in order to utilize more prior structures of the sparse vector.

3.3.1 Sparse Model

Suppose we discretize the extent of feasible Doppler shifts into N_β grid points as $\{\beta_i, i = 0, 1, \dots, N_\beta - 1\}$. Then, we can remodel (3.8) as

$$y_l(n) = a_l \tilde{\boldsymbol{\phi}}_l(n)^T \boldsymbol{\zeta}_l + e_l(n), \quad (3.12)$$

where

- $\tilde{\boldsymbol{\phi}}_l(n) = [\phi_{l0}(n), \phi_{l1}(n), \dots, \phi_{l(N_\beta-1)}(n)]^T$ represents an equivalent sparsity-based modeling of $\boldsymbol{\phi}_l(n)$;
- $\boldsymbol{\zeta}_l = [\zeta_{l0}, \zeta_{l1}, \dots, \zeta_{l(N_\beta-1)}]^T$ is an $N_\beta \times 1$ sparse vector, having $P (\ll N_\beta)$ nonzero entries corresponding to the true target scattering coefficients, i.e.,

$$\zeta_{li} = \begin{cases} x_{lp} & \text{if } i = p, \\ 0 & \text{otherwise.} \end{cases} \quad (3.13)$$

Using the formulation of (3.12) and following the approach presented in Sect. 3.2.2 to obtain (3.10) from (3.8), we deduce a sparse-measurement model as

$$\mathbf{y} = \tilde{\boldsymbol{\Psi}} \boldsymbol{\zeta} + \mathbf{e}, \quad (3.14)$$

where

- $\tilde{\boldsymbol{\Psi}} = [(\mathbf{A}\tilde{\boldsymbol{\Phi}}(0))^T \dots (\mathbf{A}\tilde{\boldsymbol{\Phi}}(N-1))^T]^T$ is an $LN \times LN_\beta$ sparse-measurement matrix containing all the viable Doppler information in terms of the $L \times LN_\beta$ dimensional matrices $\tilde{\boldsymbol{\Phi}}(n) = \text{blkdiag}(\tilde{\boldsymbol{\phi}}_0(n)^T, \tilde{\boldsymbol{\phi}}_1(n)^T, \dots, \tilde{\boldsymbol{\phi}}_{L-1}(n)^T)$;
- $\boldsymbol{\zeta} = [\boldsymbol{\zeta}_0^T, \boldsymbol{\zeta}_1^T, \dots, \boldsymbol{\zeta}_{L-1}^T]^T$ is an $LN_\beta \times 1$ sparse-vector that has LP nonzero entries representing the scattering coefficients of the target along all the P received paths and L subcarriers.

3.3.2 Sparse Recovery

The goal of a sparse-reconstruction algorithm is to estimate the vector $\boldsymbol{\zeta}$ from the noisy measurement \mathbf{y} of (3.14) by exploiting the sparsity. One of the most popular

approaches of sparse-signal recovery is the Dantzig selector [8], which provides an estimate of ζ as a solution to the following ℓ_1 -regularization problem:

$$\min_{\mathbf{z} \in \mathbb{C}^{LN_\beta}} \|\mathbf{z}\|_1 \quad \text{subject to} \quad \|\tilde{\Psi}^H(\mathbf{y} - \tilde{\Psi}\mathbf{z})\|_\infty \leq \lambda \cdot \sigma, \quad (3.15)$$

where $\lambda = \sqrt{2 \log(LN_\beta)}$ is a control parameter that ensures that the residual $(\mathbf{y} - \tilde{\Psi}\mathbf{z})$ is within the noise level and $\sigma = \sqrt{\text{tr}(\Sigma)}/L$.

However, from the construction of ζ in (3.14), i.e., from $\zeta = [\zeta_0^T, \zeta_1^T, \dots, \zeta_{L-1}^T]^T$ we observe that each $\zeta_l, l = 0, 1, \dots, L-1$, is sparse with sparsity level P . Furthermore, the system matrix $\tilde{\Psi}$ in (3.14) can be expressed as

$$\tilde{\Psi} = [\tilde{\Psi}_0 \quad \tilde{\Psi}_1 \quad \dots \quad \tilde{\Psi}_{L-1}], \quad (3.16)$$

where each block-matrix of dimension $LN \times N_\beta$ is orthogonal to any other block-matrix, i.e., $\tilde{\Psi}_{l_1}^H \tilde{\Psi}_{l_2} = \mathbf{0}$ for $l_1 \neq l_2$.

To exploit this additional structure in the sparse-recovery algorithm, we propose a concentrated estimate $\hat{\zeta} = [\hat{\zeta}_0^T, \hat{\zeta}_1^T, \dots, \hat{\zeta}_{L-1}^T]^T$ which is obtained from the individual solutions, $\hat{\zeta}_l$ s, of the L small Dantzig selectors:

$$\min_{\mathbf{z}_l \in \mathbb{C}^{N_\beta}} \|\mathbf{z}_l\|_1 \quad \text{subject to} \quad \|\tilde{\Psi}_l^H(\mathbf{y} - \tilde{\Psi}_l \mathbf{z}_l)\|_\infty \leq \lambda_l \cdot \sigma \quad \text{for } l = 0, 1, \dots, L-1, \quad (3.17)$$

where $\lambda_l = \sqrt{2 \log(N_\beta)}$. As (3.17) exploits more prior structures of the sparse vector, it provides improved performances over (3.15) both in terms of computational-time and estimation-accuracy [48].

3.4 Adaptive Waveform Design

In this section, we develop an adaptive waveform design technique based on a multi-objective optimization (MOO) approach. To improve the detection performance, we propose to maximize the Mahalanobis distance which quantifies the distance between two distributions involved in the detection problem. However, in practice, the computation of the Mahalanobis distance requires estimations of the target scattering-response, target velocity, and noise covariance matrix. So, in addition to maximizing the Mahalanobis distance, we intend to increase the estimation-accuracy by minimizing a weighted trace of the CRB matrix computed for the unknown parameters. Furthermore, the formulation of sparse-measurement model allows us to construct and solve another optimization problem that minimizes the upper bound on the sparse-estimation error for improving the efficiency of sparse-recovery. In the following, we first present in detail these three single-objective functions and then describe the MOO problem.

3.4.1 Maximizing the Mahalanobis Distance

To decide whether a target is present or not in the range cell under test, the standard procedure is to construct a decision problem that chooses between two possible hypotheses: the null hypothesis \mathcal{H}_0 (target-free hypothesis) or the alternate hypothesis \mathcal{H}_1 (target-present hypothesis). The problem can be expressed as

$$\begin{cases} \mathcal{H}_0 : \mathbf{y} = \mathbf{e}, \\ \mathcal{H}_1 : \mathbf{y} = \Psi \mathbf{x} + \mathbf{e}, \end{cases} \quad (3.18)$$

and the measurement \mathbf{y} is distributed as $\mathbb{C}\mathcal{N}_{LN}(\mathbf{0}, \mathbf{I}_N \otimes \Sigma)$ or $\mathbb{C}\mathcal{N}_{LN}(\Psi \mathbf{x}, \mathbf{I}_N \otimes \Sigma)$. To distinguish between these two distributions, one standard measure is the squared Mahalanobis distance, defined as

$$\begin{aligned} d^2 &= \mathbf{x}^H \Psi^H (\mathbf{I}_N \otimes \Sigma)^{-1} \Psi \mathbf{x} \\ &= \sum_{n=0}^{N-1} \mathbf{x}^H \Phi(n)^H \mathbf{A}^H \Sigma^{-1} \mathbf{A} \Phi(n) \mathbf{x}. \end{aligned} \quad (3.19)$$

Then, to maximize the detection performance, we can formulate an optimization problem as

$$\mathbf{a}^{(1)} = \arg \max_{\mathbf{a} \in \mathbb{C}^L} \left[\sum_{n=0}^{N-1} \mathbf{x}^H \Phi(n)^H \mathbf{A}^H \Sigma^{-1} \mathbf{A} \Phi(n) \mathbf{x} \right] \quad \text{subject to} \quad \mathbf{a}^H \mathbf{a} = 1. \quad (3.20)$$

After some algebraic manipulations (see [48, App. C]) we can rewrite this problem as

$$\mathbf{a}^{(1)} = \arg \max_{\mathbf{a} \in \mathbb{C}^L} \mathbf{a}^H \left[\sum_{n=0}^{N-1} (\Phi(n) \mathbf{x} \mathbf{x}^H \Phi(n)^H)^T \odot \Sigma^{-1} \right] \mathbf{a} \quad \text{subject to} \quad \mathbf{a}^H \mathbf{a} = 1. \quad (3.21)$$

Hence, the optimization problem reduces to a simple eigenvalue-eigenvector problem, and the solution of (3.21) is the eigenvector corresponding to the largest eigenvalue of

$$\left[\sum_{n=0}^{N-1} (\Phi(n) \mathbf{x} \mathbf{x}^H \Phi(n)^H)^T \odot \Sigma^{-1} \right].$$

However in practical scenarios, to obtain $\mathbf{a}^{(1)}$ by solving (3.21), we need to estimate the values of \mathbf{v} , \mathbf{x} , and Σ .

3.4.2 Minimizing the Weighted Trace of CRB Matrix

To characterize the accuracy of the estimation process, we compute the CRBs on the target velocity, \mathbf{v} , and scattering-parameters, \mathbf{x} . For mathematical simplicity, we

assume here that the noise covariance matrix, Σ , is known. The motivation behind considering the CRB as the performance measure is that it represents a universal lower bound on the variance of all unbiased estimators of a set of parameters. If an estimator is unbiased and attains the CRB, then it is said to be *efficient* in using the measured data. Alternatively, even if there is no unbiased estimator that attains the CRB, finding this lower bound provides a useful theoretical benchmark against which we can compare the performance of any other unbiased estimator [26, Chap. 3].

Considering a ground-moving target with $\mathbf{v} = v_x \hat{i} + v_y \hat{j}$, we define two sets of vectors $\mathbf{g}_l(n)$ s and $\mathbf{h}_l(n)$ s, for $l = 0, \dots, L-1$, $n = 0, \dots, N-1$, respectively as

$$\begin{aligned}\mathbf{g}_l(n) &= (j4\pi f_l n T/c)[u_{x,1}, u_{x,2}, \dots, u_{x,P}]^T, \\ \mathbf{h}_l(n) &= (j4\pi f_l n T/c)[u_{y,1}, u_{y,2}, \dots, u_{y,P}]^T,\end{aligned}$$

where $\{u_{x,p}, u_{y,p}\}$ are the components of \mathbf{u}_p , i.e., $\mathbf{u}_p = u_{x,p} \hat{i} + u_{y,p} \hat{j}$ for $p = 1, 2, \dots, P$. Then, denoting the unknown parameter-vector as $\boldsymbol{\theta} = [\boldsymbol{\eta}^T, \mathbf{x}^T]^T$, where $\boldsymbol{\eta} = [v_x, v_y]^T$, we get the partial-derivative matrices as

$$\mathbf{D}_\boldsymbol{\eta} \triangleq \frac{\partial(\Psi \mathbf{x})}{\partial \boldsymbol{\eta}} = \left[\frac{\partial \Psi}{\partial v_x} \mathbf{x} \quad \frac{\partial \Psi}{\partial v_y} \mathbf{x} \right], \quad (3.22)$$

$$\mathbf{D}_\mathbf{x} \triangleq \frac{\partial(\Psi \mathbf{x})}{\partial \mathbf{x}} = \Psi, \quad (3.23)$$

where

$$\begin{aligned}\frac{\partial \Psi}{\partial v_x} &= \left[\left(\mathbf{A} \frac{\partial \Phi(0)}{\partial v_x} \right)^T \dots \left(\mathbf{A} \frac{\partial \Phi(N-1)}{\partial v_x} \right)^T \right]^T, \\ \frac{\partial \Phi(n)}{\partial v_x} &= \text{blkdiag}((\boldsymbol{\phi}_0(n) \odot \mathbf{g}_0(n))^T, \dots, (\boldsymbol{\phi}_{L-1}(n) \odot \mathbf{g}_{L-1}(n))^T),\end{aligned} \quad (3.24)$$

and

$$\begin{aligned}\frac{\partial \Psi}{\partial v_y} &= \left[\left(\mathbf{A} \frac{\partial \Phi(0)}{\partial v_y} \right)^T \dots \left(\mathbf{A} \frac{\partial \Phi(N-1)}{\partial v_y} \right)^T \right]^T, \\ \frac{\partial \Phi(n)}{\partial v_y} &= \text{blkdiag}((\boldsymbol{\phi}_0(n) \odot \mathbf{h}_0(n))^T, \dots, (\boldsymbol{\phi}_{L-1}(n) \odot \mathbf{h}_{L-1}(n))^T).\end{aligned} \quad (3.25)$$

Subsequently, we calculate the CRB on $\boldsymbol{\theta}$ as

$$\mathbf{CRB}(\boldsymbol{\theta}) = \begin{bmatrix} \mathbf{CRB}_{\boldsymbol{\eta}\boldsymbol{\eta}} & \mathbf{CRB}_{\boldsymbol{\eta}\mathbf{x}} \\ \mathbf{CRB}_{\mathbf{x}\boldsymbol{\eta}} & \mathbf{CRB}_{\mathbf{x}\mathbf{x}} \end{bmatrix} = \begin{bmatrix} \mathbf{J}_{\boldsymbol{\eta}\boldsymbol{\eta}} & \mathbf{J}_{\boldsymbol{\eta}\mathbf{x}} \\ \mathbf{J}_{\mathbf{x}\boldsymbol{\eta}} & \mathbf{J}_{\mathbf{x}\mathbf{x}} \end{bmatrix}^{-1}, \quad (3.26)$$

where the elements of the Fisher information matrix (FIM) are expressed as

$$\begin{aligned} \mathbf{J}_{\eta\eta} &= 2 \operatorname{Re}\{\mathbf{D}_\eta^H (\mathbf{I}_N \otimes \boldsymbol{\Sigma})^{-1} \mathbf{D}_\eta\} \\ &= \sum_{n=0}^{N-1} 2 \operatorname{Re}\left\{\left[\frac{\partial \boldsymbol{\Phi}(n)}{\partial v_x} \mathbf{x} \frac{\partial \boldsymbol{\Phi}(n)}{\partial v_y} \mathbf{x}\right]^H \mathbf{A}^H \boldsymbol{\Sigma}^{-1} \mathbf{A} \left[\frac{\partial \boldsymbol{\Phi}(n)}{\partial v_x} \mathbf{x} \frac{\partial \boldsymbol{\Phi}(n)}{\partial v_y} \mathbf{x}\right]\right\}, \end{aligned} \quad (3.27)$$

$$\begin{aligned} \mathbf{J}_{\eta\mathbf{x}} &= 2 \operatorname{Re}\{\mathbf{D}_\eta^H (\mathbf{I}_N \otimes \boldsymbol{\Sigma})^{-1} \mathbf{D}_\mathbf{x}\} \\ &= \sum_{n=0}^{N-1} 2 \operatorname{Re}\left\{\left[\frac{\partial \boldsymbol{\Phi}(n)}{\partial v_x} \mathbf{x} \frac{\partial \boldsymbol{\Phi}(n)}{\partial v_y} \mathbf{x}\right]^H \mathbf{A}^H \boldsymbol{\Sigma}^{-1} \mathbf{A} \boldsymbol{\Phi}(n)\right\}, \end{aligned} \quad (3.28)$$

$$\begin{aligned} \mathbf{J}_{\mathbf{x}\eta} &= 2 \operatorname{Re}\{\mathbf{D}_\mathbf{x}^H (\mathbf{I}_N \otimes \boldsymbol{\Sigma})^{-1} \mathbf{D}_\eta\} \\ &= \sum_{n=0}^{N-1} 2 \operatorname{Re}\left\{\boldsymbol{\Phi}(n)^H \mathbf{A}^H \boldsymbol{\Sigma}^{-1} \mathbf{A} \left[\frac{\partial \boldsymbol{\Phi}(n)}{\partial v_x} \mathbf{x} \frac{\partial \boldsymbol{\Phi}(n)}{\partial v_y} \mathbf{x}\right]\right\}, \end{aligned} \quad (3.29)$$

$$\mathbf{J}_{\mathbf{x}\mathbf{x}} = 2 \operatorname{Re}\{\mathbf{D}_\mathbf{x}^H (\mathbf{I}_N \otimes \boldsymbol{\Sigma})^{-1} \mathbf{D}_\mathbf{x}\} = \sum_{n=0}^{N-1} 2 \operatorname{Re}\{\boldsymbol{\Phi}(n)^H \mathbf{A}^H \boldsymbol{\Sigma}^{-1} \mathbf{A} \boldsymbol{\Phi}(n)\}. \quad (3.30)$$

Now, to obtain a scalar objective function that summarizes the CRB matrix, several optimality criteria can be considered. For example, A -optimality criterion employs the trace, D -optimality uses the determinant, and E -optimality computes the maximum eigenvalue of the CRB matrix [6, Chap. 7.5.2]. However, due to the different physical characteristics of $\boldsymbol{\eta}$ and \mathbf{x} , the variances of their estimators may differ in several orders of magnitude and units. Therefore, we construct an objective function to design the OFDM spectral-parameters that minimizes a weighted summation of the traces of individual CRBs on $\boldsymbol{\eta}$ and \mathbf{x} as

$$\mathbf{a}^{(2)} = \arg \min_{\mathbf{a} \in \mathbb{C}^L} c_\eta \operatorname{tr}(\mathbf{CRB}_{\eta\eta}) + c_x \operatorname{tr}(\mathbf{CRB}_{\mathbf{x}\mathbf{x}}) \quad \text{subject to} \quad \mathbf{a}^H \mathbf{a} = 1, \quad (3.31)$$

where c_η and c_x are the weighting parameters.

3.4.3 Minimizing the Upper Bound on Sparse Error

Many functions of the system matrix $\tilde{\Psi}$ have been proposed to analyze the performance of methods used to recover $\boldsymbol{\zeta}$ from \mathbf{y} , the most popular measure being the restricted isometry constant (RIC). However, for a given arbitrary matrix, the computation of RIC is extremely difficult. Therefore, in [52] we proposed a new, easily computable measure, ℓ_1 -constrained minimal singular value (ℓ_1 -CMSV) of $\tilde{\Psi}$, to assess the reconstruction performance of an ℓ_1 -based algorithm. According to [52, Def. 3], we define the ℓ_1 -CMSV of $\tilde{\Psi}$ as

$$\rho_s(\tilde{\Psi}) = \min_{\boldsymbol{\zeta} \neq \mathbf{0}, s_1(\boldsymbol{\zeta}) \leq s} \frac{\|\tilde{\Psi} \boldsymbol{\zeta}\|_2}{\|\boldsymbol{\zeta}\|_2}, \quad \text{for any } s \in [1, LN_\beta], \quad (3.32)$$

and

$$s_1(\boldsymbol{\zeta}) \triangleq \frac{\|\boldsymbol{\zeta}\|_1^2}{\|\boldsymbol{\zeta}\|_2^2} \leq \|\boldsymbol{\zeta}\|_0. \quad (3.33)$$

Then, the performance of our decomposed Dantzig selector (DS) approach in (3.17) is given by the following theorem:

Theorem 3.1 [48] *Suppose $\boldsymbol{\zeta} \in \mathbb{C}^{LN_\beta}$ is an LP -sparse vector having an additional structure as presented in (3.14), with each $\boldsymbol{\zeta}_l \in \mathbb{C}^{N_\beta}$ being a P -sparse vector, and (3.14) is the measurement model. Then, with high probability, the concentrated solution $\widehat{\boldsymbol{\zeta}} = [\widehat{\boldsymbol{\zeta}}_0^T, \widehat{\boldsymbol{\zeta}}_1^T, \dots, \widehat{\boldsymbol{\zeta}}_{L-1}^T]^T$ of (3.17) satisfies*

$$\|\widehat{\boldsymbol{\zeta}} - \boldsymbol{\zeta}\|_2 \leq 4 \sqrt{\sum_{l=0}^{L-1} \frac{\lambda_l^2 P \sigma^2}{a_l^4 \rho_{4P}^4(\widetilde{\boldsymbol{\Phi}}_l)}}, \quad (3.34)$$

where $\widetilde{\boldsymbol{\Phi}}_l$ is related with $\widetilde{\boldsymbol{\Psi}}_l$ of (3.16) as $\widetilde{\boldsymbol{\Psi}}_l = a_l \widetilde{\boldsymbol{\Phi}}_l$. More specifically, if $\lambda_l = \sqrt{2(1+q) \log(N_\beta)}$ for each $q \geq 0$ is used in (3.17), then the bound holds with probability greater than $1 - L(\sqrt{\pi(1+q) \log(N_\beta)} \cdot (N_\beta)^q)^{-1}$.

Proof See [48]. □

To minimize the upper bound on the sparse-estimation error, we formulate an optimization problem as

$$\mathbf{a}^{(3)} = \arg \min_{\mathbf{a} \in \mathbb{C}^L} \sum_{l=0}^{L-1} \frac{\lambda_l^2 P \sigma^2}{a_l^4 \rho_{4P}^4(\widetilde{\boldsymbol{\Phi}}_l)} \quad \text{subject to} \quad \mathbf{a}^H \mathbf{a} = 1. \quad (3.35)$$

Using the Lagrange-multiplier approach, we can easily obtain the solution of (3.35) as

$$a_l^{(3)} = \sqrt{\frac{(2\alpha_l)^{1/3}}{\sum_{l=0}^{L-1} (2\alpha_l)^{1/3}}}, \quad \text{where } \alpha_l = \frac{\lambda_l^2 P \sigma^2}{\rho_{4P}^4(\widetilde{\boldsymbol{\Phi}}_l)}, \quad (3.36)$$

for $l = 0, 1, \dots, L-1$.

However, the computation of $\rho_{4P}(\widetilde{\boldsymbol{\Phi}}_l)$ is difficult with the complex variables. Therefore, we use a computable lower bound on $\rho_{4P}(\widetilde{\boldsymbol{\Phi}}_l)$, defined as

$$\rho_{8P}(\boldsymbol{\Gamma}_l) \leq \rho_{4P}(\widetilde{\boldsymbol{\Phi}}_l), \quad (3.37)$$

where

$$\boldsymbol{\Gamma}_l^T \boldsymbol{\Gamma}_l = \begin{bmatrix} \boldsymbol{\Gamma}_1^T \boldsymbol{\Gamma}_1 + \boldsymbol{\Gamma}_2^T \boldsymbol{\Gamma}_2 & \mathbf{0} \\ \mathbf{0} & \boldsymbol{\Gamma}_1^T \boldsymbol{\Gamma}_1 + \boldsymbol{\Gamma}_2^T \boldsymbol{\Gamma}_2 \end{bmatrix}, \quad \boldsymbol{\Gamma}_1 = \text{Re } \widetilde{\boldsymbol{\Phi}}_l, \boldsymbol{\Gamma}_2 = \text{Im } \widetilde{\boldsymbol{\Phi}}_l. \quad (3.38)$$

Then, similar to (3.36), we can obtain the optimal OFDM spectral-parameters as

$$a_l^{(3)} = \sqrt{\frac{(2\tilde{\alpha}_l)^{1/3}}{\sum_{l=0}^{L-1} (2\tilde{\alpha}_l)^{1/3}}}, \quad \text{where } \tilde{\alpha}_l = \frac{\lambda_l^2 P \sigma^2}{\rho_{8p}^4(\Gamma_l)}, \quad (3.39)$$

for $l = 0, 1, \dots, L - 1$.

3.4.4 Multi-objective Optimization

From the discussion of the previous subsections, we notice that if the solution of (3.21) is used we would get an improved detection performance provided that we know a-priori the values of the target velocity, scattering-response, and noise covariance matrix. Alternatively, by solving (3.31), we could improve the performances of the underlying estimation problems for the target response and velocity. Furthermore, if we were to use the solution of (3.39), we would achieve an efficient sparse-recovery result when we address the detection problem from a sparse-estimation perspective. Hence, based on these arguments, we devise a constrained MOO problem to design the spectral parameters of the OFDM waveform such that simultaneously (i) the squared Mahalanobis distance of the detection problem is maximized, (ii) the weighted summation of the traces of CRB matrices for $\boldsymbol{\eta}$ and \mathbf{x} is minimized, and (iii) the upper bound on the sparse-estimation error of the equivalent sparse-recovery approach is minimized. Mathematically, this is represented as

$$\mathbf{a}_{\text{opt}} = \begin{cases} \arg \max_{\mathbf{a} \in \mathbb{C}^L} \mathbf{a}^H [\sum_{n=0}^{N-1} (\tilde{\boldsymbol{\Phi}}(n) \boldsymbol{\zeta} \boldsymbol{\zeta}^H \tilde{\boldsymbol{\Phi}}(n)^H)^T \odot \boldsymbol{\Sigma}^{-1}] \mathbf{a}, \\ \arg \min_{\mathbf{a} \in \mathbb{C}^L} c_{\boldsymbol{\eta}} \text{tr}(\mathbf{CRB}_{\boldsymbol{\eta}\boldsymbol{\eta}}) + c_{\mathbf{x}} \text{tr}(\mathbf{CRB}_{\mathbf{x}\mathbf{x}}), \\ \arg \min_{\mathbf{a} \in \mathbb{C}^L} \sum_{l=0}^{L-1} \frac{\lambda_l^2 P \sigma^2}{a_l^4 \rho_{8p}^4(\Gamma_l)}, \end{cases} \quad (3.40)$$

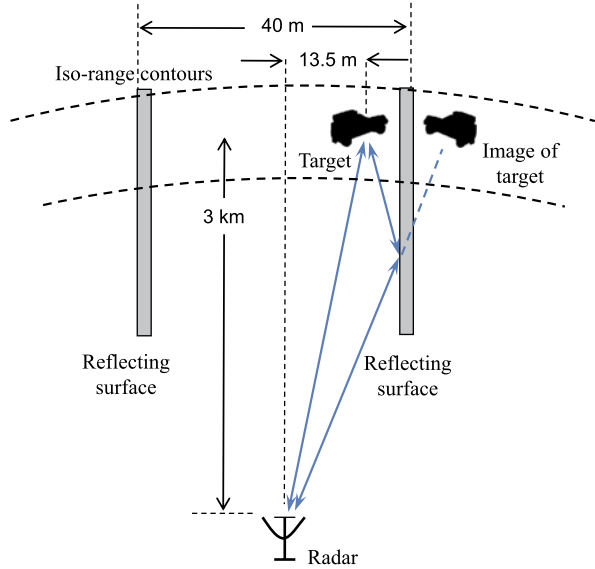
subject to $\mathbf{a}^H \mathbf{a} = 1$.

We employ the standard nondominated sorting genetic algorithm II (NSGA-II) to solve our MOO problem, after modifying it to incorporate the constraint $\mathbf{a}^H \mathbf{a} = 1$ that needs to be imposed upon the solutions.

3.5 Numerical Results

In this section, we present the results of several numerical examples to discuss the solutions of the MOO problem and to demonstrate the performance improvement due to the adaptive OFDM-waveform design technique. For simplicity, we consider a 2D scenario, as shown in Fig. 3.3, where both the radar and target are in the same plane. Our analyses can easily be extended to 3D scenarios. First, we provide a description of the simulation setup and then discuss different numerical results.

Fig. 3.3 A schematic representation of the multipath scenario considered in the numerical examples



- *Target and multipath parameters:*

- Throughout a given coherent processing interval (CPI), the target remained within a particular range cell. We simulated the situation of a range cell that is at a distance of 3 km from the radar (positioned at the origin).
- The target was 13.5 m east from the center line, moving with velocity $\mathbf{v} = (35/\sqrt{2})(\hat{i} + \hat{j})$ m/s.
- There were two different paths between the target and radar: one direct and one reflected, subtending angles of 0.26° and 0.51° , respectively, with respect to the radar. Hence, the target manifests two relative speeds of $\langle \mathbf{v}, \mathbf{u}_p \rangle = 24.86$ and 24.53 m/s at the radar receiver.
- The scattering coefficients of the target, \mathbf{x} , were varied to simulate two scenarios having different energy-distributions across different subchannels. For example, Scenario I had the strongest target-reflectivity on the second subcarrier with $x_{l,d}^{(1)} = [2, 4, 1]^T$ and $x_{l,r}^{(1)} = [1, 2, 0.5]^T$ representing the scattering coefficients along the direct and reflected paths, respectively. On the other hand, in Scenario II we considered the strongest target-reflectivity along the first subcarrier with $x_{l,d}^{(1)} = [3, 1, 2]^T$ and $x_{l,r}^{(1)} = [1.5, 0.5, 1]^T$.

However, for the purpose of a fair comparison, we scaled the target-scattering coefficients to ensure a constant signal-to-noise ratio (SNR), defined as

$$\text{SNR} = \frac{\|\mathbf{x}\|^2}{\text{tr}(\boldsymbol{\Sigma})}. \quad (3.41)$$

Hence, a stronger target-reflectivity along a certain subcarrier implied that there would be some other subcarriers with very poor target-reflectivities.

- *Radar parameters:*

- Carrier frequency $f_c = 1$ GHz;
- Available bandwidth $B = 10$ MHz;
- Number of OFDM subcarriers $L = 3$;
- Subcarrier spacing of $\Delta f = B/(L + 1) = 2.5$ MHz;
- Pulse width $T_p = 1/\Delta f = 400$ ns;
- Pulse repetition interval $T = 4$ ms;
- Number of coherent pulses $N = 20$;
- All the transmit OFDM weights were equal, i.e., $a_l = 1/\sqrt{L} \forall l$.

- *Simulation parameters:*

To apply a sparse estimation, we partitioned the viable relative speeds from 24.5 to 25 m/s with steps of 0.05 m/s. We generated the noise samples from a $\mathcal{C}\mathcal{N}_{LN}(\mathbf{0}, \mathbf{I}_N \otimes \mathbf{\Sigma})$ distribution with $\mathbf{\Sigma} = [1, 0.1, 0.01; 0.1, 1, 0.1; 0.01, 0.1, 1]$. Hence, for all the results presented in this section we ensured a constant noise-power distribution among all the subchannels.

To solve the MOO problem (3.40), we employed the NSGA-II with the following parameters: population size = 1000, number of generations = 100, crossover probability = 0.9, and mutation probability = 0.1. The initial population of 1000 different values of \mathbf{a} were generated randomly, but ensuring that the total-energy constraint $\mathbf{a}^H \mathbf{a} = 1$ was satisfied. Furthermore, at each generation of the NSGA-II, we imposed the total-energy constraint on the children-chromosomes by introducing an ‘if-statement’ in the ‘genetic-operator’ portion of the NSGA-II code. However, satisfying the hard-equality constraint $\mathbf{a}^H \mathbf{a} = 1$ was difficult to simulate due to the numerical precision errors. That is why we relaxed it with a softer constraint by considering $0.999 \leq \mathbf{a}^H \mathbf{a} \leq 1.001$.

3.5.1 Results of the MOO Problem

The results of the MOO problem are depicted in Figs. 3.4, 3.5 and Figs. 3.6, 3.7 for the target Scenarios I and II, respectively. We maintained a fixed SNR of 0 dB for these simulations. The initial population of 1000 different values of \mathbf{a} were generated randomly. Considering a Cartesian coordinate system with $|a_{1_{\text{opt}}}|$, $|a_{2_{\text{opt}}}|$, and $|a_{3_{\text{opt}}}|$ as the axes, the initial population is represented on the surface of a sphere restricted to the first octant, as shown by circles in Figs. 3.4(a) and 3.6(a) for the two different target scenarios. The values of the associated objective functions are also indicated by circles respectively in Figs. 3.4(b) and 3.6(b), whose coordinate systems are constructed with the three objective functions representing the axes on the logarithmic scales.

We represent the Pareto-optimal solutions by squares in Figs. 3.4(a) and 3.6(a) and the associated Pareto-optimal objective values by squares in Figs. 3.4(b) and 3.6(b), for the Scenarios I and II, respectively. In Scenario I, when the target had the strongest reflectivity along the second subcarrier, we got the optimal solutions varying from $|\mathbf{a}_{\text{opt}}| = [0.6189, 0.6691, 0.4119]^T$ to $|\mathbf{a}_{\text{opt}}| = [0, 1, 0]^T$ on an

Fig. 3.4 Results of the NSGA-II in Scenario I: (a) optimal solutions and (b) values of the objective functions at the zeroth and 100th generations are respectively represented by circles and squares

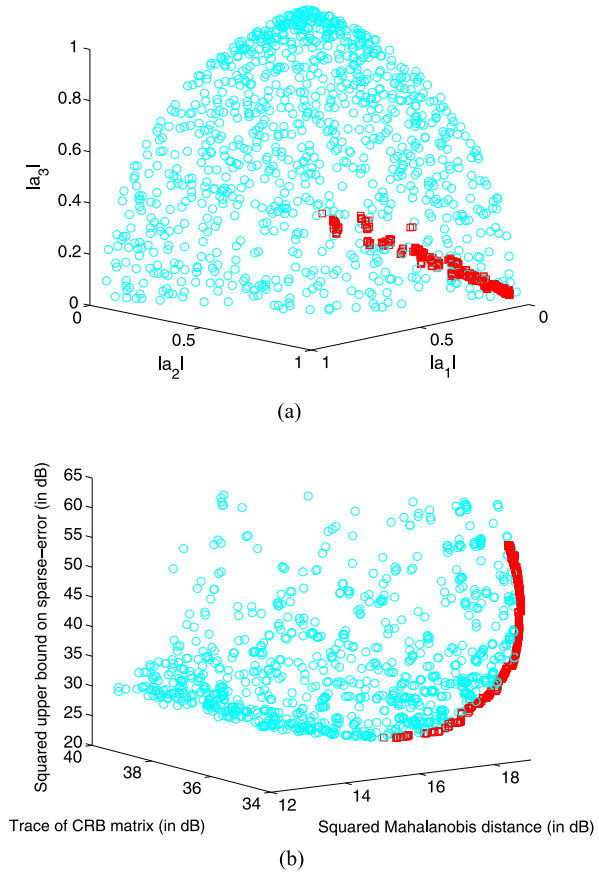
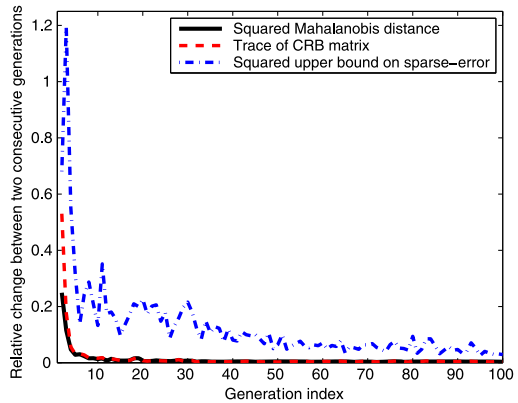
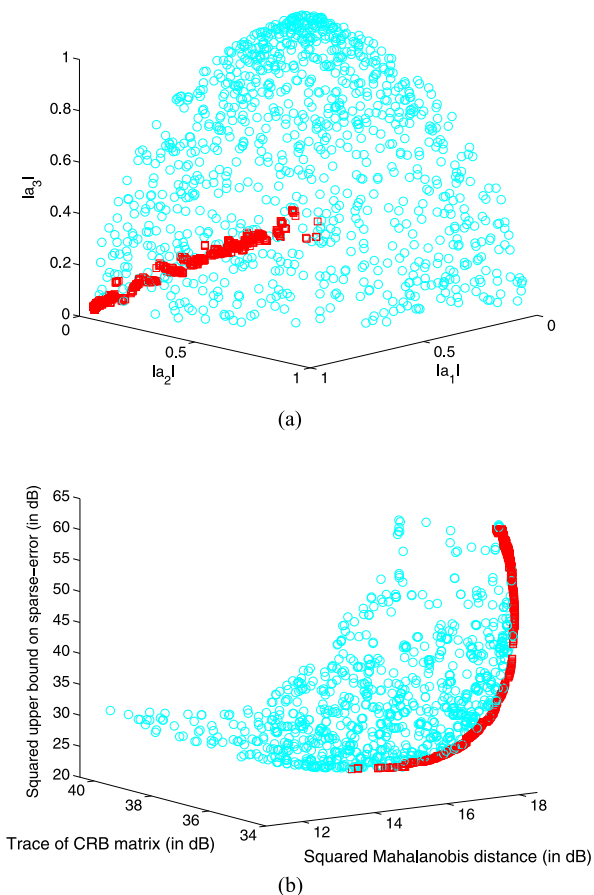


Fig. 3.5 Convergence of the objective functions to the Pareto-optimal values in Scenario I



approximately straight-line locus subtended on the surface of a sphere. It is important to note here that if we had solved only (3.39) to minimize the upper bound on the sparse-error, then the solution would have been $|\mathbf{a}^{(3)}| = [0.6261, 0.6578, 0.4187]^T$;

Fig. 3.6 Results of the NSGA-II in Scenario II: (a) optimal solutions and (b) values of the objective functions at the zeroth and 100th generations are respectively represented by circles and squares

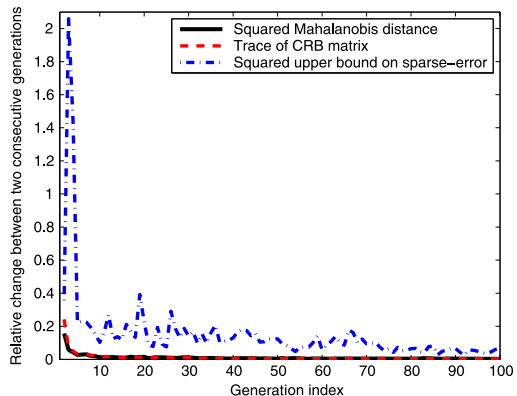


whereas an effort to obtain the solution of only (3.21) would result in $|\mathbf{a}^{(1)}| = [0.0652, 0.9975, 0.0262]^T$. This implies that Pareto-optimal solutions provide a set of compromised solutions varying in between two extrema that are approximately equal to the individual solutions of the objective functions when solved separately.

Similarly, for the Scenario II which had the strongest target-reflectivity along the first subcarrier, we found that the MOO-solutions lied on an approximately straight-line locus drawn on the surface of a sphere and varied from $|\mathbf{a}_{\text{opt}}| = [0.6339, 0.6510, 0.4182]^T$ to $|\mathbf{a}_{\text{opt}}| = [1, 0, 0]^T$. Comparing with the individual solutions of the objective functions in Scenario II, we noticed that (3.21) resulted in $|\mathbf{a}^{(1)}| = [0.9992, 0.0374, 0.0015]^T$; whereas the solution of (3.39) still produced $|\mathbf{a}^{(3)}| = [0.6261, 0.6578, 0.4187]^T$ because it was a function of the system matrix $\tilde{\Psi}$ only.

In addition, to assess the speed of convergence to these Pareto-optimal solutions, in Figs. 3.5 and 3.7 we depict the relative change in values of the three objective functions at different generation indices for both the target scenarios under con-

Fig. 3.7 Convergence of the objective functions to the Pareto-optimal values in Scenario II



sideration. If $\mathbf{o}_j(k-1)$ and $\mathbf{o}_j(k)$, for $j = 1, 2, 3, k = 2, 3, \dots, 100$, denote two vectors of objective-functions respectively computed at the $(k-1)$ th and k th generations over the entire population, then their relative changes were calculated as $\|\mathbf{o}_j(k) - \mathbf{o}_j(k-1)\|/\|\mathbf{o}_j(k)\|$. It is quiet evident from these plots that the Pareto-optimal solutions were reached very quickly even within the tenth generation, particularly for the first two objective functions (3.21) and (3.31).

3.5.2 Improvement in Detection and Estimation Performance

We demonstrate the performance improvement due to the adaptive waveform design at several SNR values in terms of the squared Mahalanobis distance, weighted trace of CRB matrix, and squared upper bound on sparse-error. These results are shown in Figs. 3.8 and 3.9 for the target Scenarios I and II, respectively. As we expect, the Mahalanobis-distance measure improved as we increased the SNR values, but the trace of CRB matrix decreased and the upper bound on the sparse-estimation error remained unchanged. In each figure, the red-colored lines (in total 1000 of them) represent the variations of the objective-functions, associated with the entire population of 1000 solutions; whereas the blue-colored line shows their counterparts corresponding to the fixed (nonadaptive) waveform $\mathbf{a} = 1/\sqrt{L} = [0.5774, 0.5774, 0.5774]^T$. In both the target scenarios, we found that all the Pareto-optimal solutions produced better performances, in terms of the Mahalanobis distance and trace of CRB matrix, when compared to those with the fixed waveform. However, with respect to the squared upper bound on sparse-error, only a subset of the Pareto-optimal solutions was found to show improved performance than that with the fixed waveform.

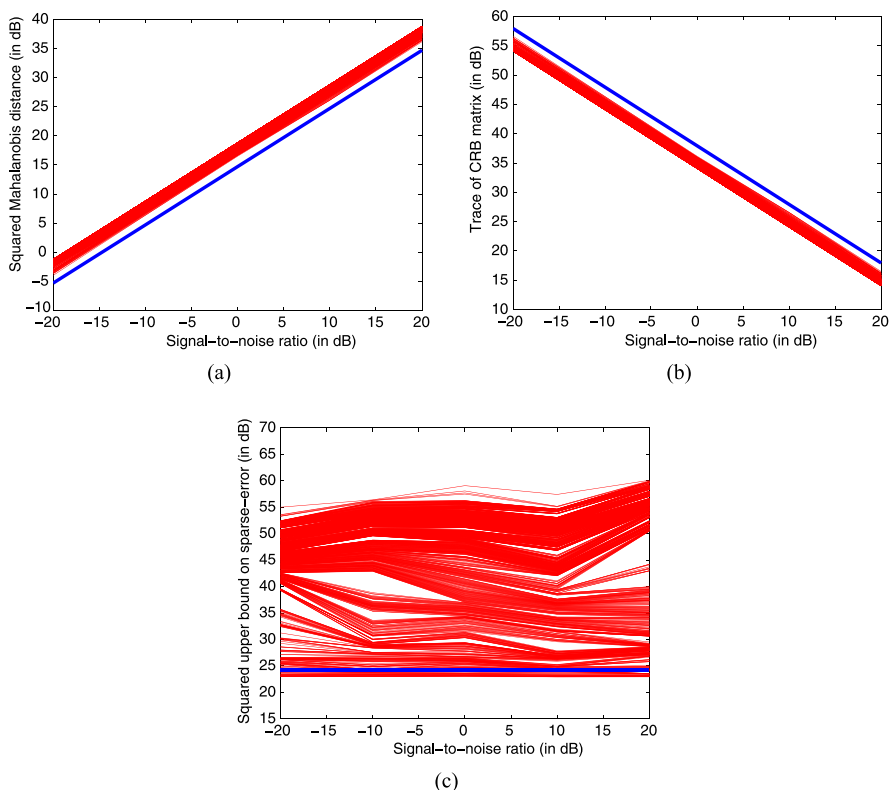


Fig. 3.8 Comparison of performances due to the fixed and adaptive waveforms in Scenario I in terms of the (a) squared Mahalanobis distance, (b) weighted trace of Cramér–Rao bound matrix, and (c) squared upper bound on sparse-error, respectively

3.5.3 Redistributions of Signal and Target Energies

To understand the reason behind the performance improvement due to the adaptive waveform design, we looked into the energy-distribution of the transmitted signal and effective target-return across different subchannels both before and after the waveform design. We used the subset of Pareto-optimal solutions that satisfied all the three objective functions at 0 dB to exemplify the results on energy-redistribution for both the target scenarios in Fig. 3.10.

We represent the effective transmit-signal energy at different subchannels as

$$\varepsilon_{s,l} = |a_l|^2, \quad \text{for } l = 0, 1, \dots, L - 1. \quad (3.42)$$

On the other hand, the effective target-returns across different subchannels are considered as

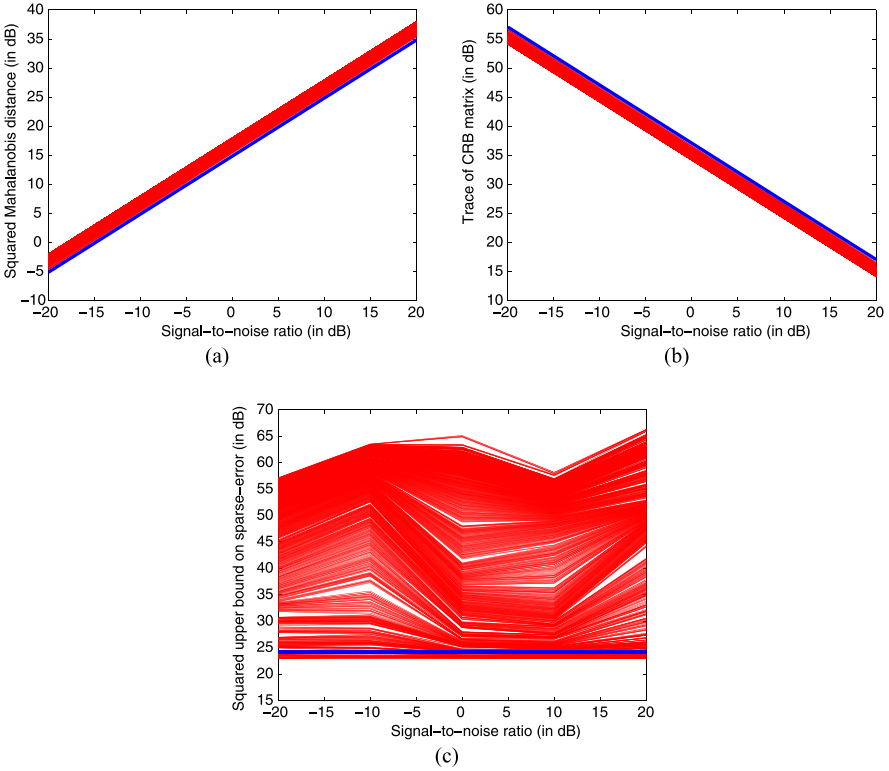


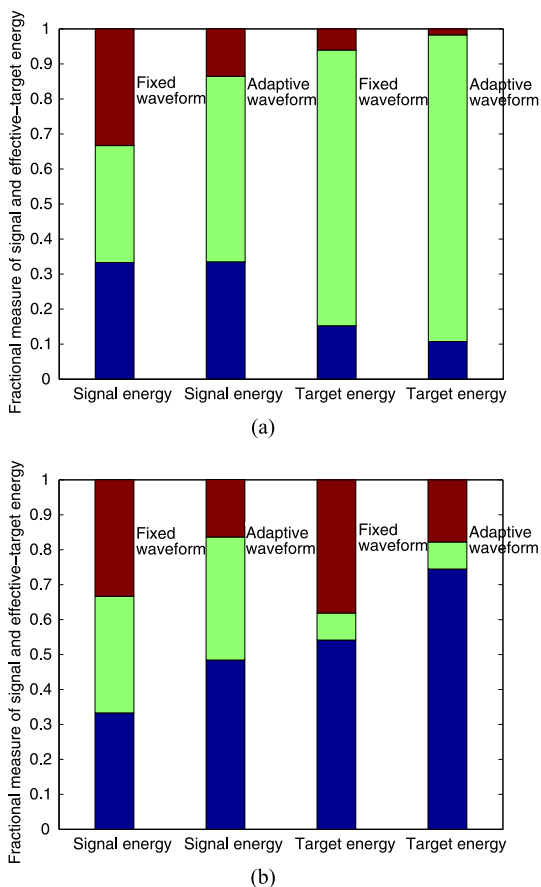
Fig. 3.9 Comparison of performances due to the fixed and adaptive waveforms in Scenario II in terms of the (a) squared Mahalanobis distance, (b) weighted trace of Cramér-Rao bound matrix, and (c) squared upper bound on sparse-error, respectively

$$\varepsilon_{T,l} = \left| \frac{1}{N} \sum_{n=0}^{N-1} a_l \phi_l(n)^T \mathbf{x}_l \right|^2, \quad \text{for } l = 0, 1, \dots, L-1. \quad (3.43)$$

Due to the adaptive design of a_l s, the set of values of $\{\varepsilon_{S,l}\}$ and $\{\varepsilon_{T,l}\}$ were different before and after the optimization process, as both of these quantities depend on the transmitted signal parameters.

In Fig. 3.10(a), we plot the values of $\{\varepsilon_{S,l}\}$ and $\{\varepsilon_{T,l}/(\sum_{l=0}^{L-1} \varepsilon_{T,l})\}$ for the target Scenario I. Noticing the two left-most vertical bars, we observe that the MOO-approach boosted up the transmitted-signal energy on the second subchannel along which the target-reflectivity was the strongest. Additionally, we found a considerable amount of energy redistribution among different subchannels for the effective target-returns, as shown in the two right-most vertical bars. With the fixed waveform, we had $\{\varepsilon_{T,l}\} = \{0.1527, 0.7868, 0.0605\}$ before the waveform design; whereas after we obtained the Pareto-optimal solution, the normalized values of $\{\varepsilon_{T,l}\}$ changed to $\{0.1075, 0.8752, 0.0173\}$. Hence, we conclude that the MOO-based optimal waveform design puts more signal-energy into that particular sub-

Fig. 3.10 The normalized energy distributions of the transmit-signal and effective target-returns across different subchannels in (a) Scenario I and (b) Scenario II



carrier at which the target response is stronger, and thus makes the effective target-return more prominent along that subcarrier.

As a further confirmation, we did a similar analysis with values of $\{\varepsilon_{S,l}\}$ and $\{\varepsilon_{T,l}/(\sum_{l=0}^{L-1} \varepsilon_{T,l})\}$ for Scenario II. Results are shown in Fig. 3.10(b). Observing the two left-most vertical bars, we again notice that the transmitted-signal energy was amplified along the first subchannel after the waveform design. The two right-most vertical bars indicate a noticeable redistribution of the effective target-energies among the different subchannels. After the adaptive waveform design, we found that the normalized values of $\{\varepsilon_{T,l}\}$ changed from $\{0.5414, 0.0775, 0.3811\}$ to $\{0.7447, 0.0775, 0.1779\}$. This reconfirms our conclusion that the Pareto-optimal waveform design tries to further enhance the stronger target-returns. Moreover, since we kept the noise-energy fixed and varied only the target-energy over different subchannels, we can extend our conclusion to assert that the solution of the Pareto-optimal design redistributes the energy of the transmitted signal by putting the most energy to that particular subcarrier in which the signal-to-noise ratio is the strongest.

3.6 Conclusions

In this chapter, we proposed a multi-objective optimization (MOO) technique to design the spectral parameters of an orthogonal frequency division multiplexing (OFDM) radar signal for detecting a moving target in the presence of multipath reflections. The use of an OFDM signal increased the frequency diversity of our system, as different scattering centers of a target resonate variably at different frequencies. We first developed a parametric OFDM measurement model for a particular range cell under test, and then converted it to a sparse model that accounted for the target returns over all possible signal paths and target velocities. In our model, the nonzero components of the sparse vector were equal to the scattering coefficients of the target at the true signal paths and target velocity. To estimate the sparse vector, we employed a collection of multiple small Dantzig selectors that utilized more prior structures of the sparse vector. In addition, we proposed a criterion to optimally design the OFDM spectral parameters for the next coherent processing interval based on the MOO approach. We applied the nondominated sorting genetic algorithm II (NSGA-II) to solve a constrained MOO problem that simultaneously optimizes three objective functions: maximizes the Mahalanobis distance to improve the detection performance, minimizes the weighted trace of the Cramér–Rao bound matrix for the unknown parameters to increase the estimation accuracy, and minimizes the upper bound on the sparse-error to improve the efficiency of the equivalent sparse-estimation approach.

We presented several numerical examples to discuss the solutions of the MOO problem and to demonstrate the achieved performance improvement due to the adaptive OFDM-waveform design. As expected, we noticed that the solutions residing on the Pareto-front were compromisable in nature and they varied in between two extrema that were approximately equal to the individual solutions of the objective functions when solved independently. We found that only a subset of the Pareto-optimal solutions produced better performance than a fixed waveform with respect to the all three objective functions. When the noise powers over different subcarriers were the same, we further inferred that the Pareto-optimal solutions put the most transmitted signal-energy to that particular subcarrier along which the signal-to-noise ratio is the strongest.

In our future work, we will extend our model to incorporate more realistic physical effects, such as diffractions and refractions, which exist, for example, due to sharp edges and corners of the buildings or rooftops in an urban environment. We will incorporate other waveform design criteria, e.g., ambiguity function and similarity constraint, into the MOO algorithm. In addition, we will validate the performance of our proposed adaptive waveform design technique with real data.

Acknowledgements This work was supported by the AFOSR Grant FA9550-11-1-0210 and ONR Grant N000140810849.

References

1. Amuso, V.J., Enslin, J.: The Strength Pareto Evolutionary Algorithm 2 (SPEA2) applied to simultaneous multi-mission waveform design. In: Proc. Intl. Waveform Diversity & Design Conf., Pisa, Italy, pp. 407–417 (2007)
2. Amuso, V.J., Josefiak, B.: A distributed object-oriented multi-mission radar waveform design implementation. In: Proc. Intl. Waveform Diversity & Design Conf., Kauai, HI, pp. 266–270 (2012)
3. Anderson, T.W.: An Introduction to Multivariate Statistical Analysis, 3rd edn. Wiley, Hoboken (2003)
4. Antonik, P., Wicks, M.C., Griffiths, H.D., Baker, C.J.: Multi-mission multi-mode waveform diversity. In: Proc. IEEE Radar Conf., Verona, NY, pp. 580–582 (2006)
5. Bell, M.: Information theory and radar waveform design. *IEEE Trans. Inf. Theory* **39**(5), 1578–1597 (1993)
6. Boyd, S.P., Vandenberghe, L.: *Convex Optimization*. Cambridge University Press, New York (2004)
7. Calderbank, R., Howard, S., Moran, B.: Waveform diversity in radar signal processing. *IEEE Signal Process. Mag.* **26**(1), 32–41 (2009)
8. Candès, E., Tao, T.: The Dantzig selector: statistical estimation when p is much larger than n . *Ann. Stat.* **35**(6), 2313–2351 (2007)
9. Candès, E.J.: The restricted isometry property and its implications for compressed sensing. *C. R. Math.* **346**(9–10), 589–592 (2008)
10. Candès, E.J., Tao, T.: Decoding by linear programming. *IEEE Trans. Inf. Theory* **51**(12), 4203–4215 (2005)
11. Coello, C.A.C., Lamont, G.B., Veldhuizen, D.A.V.: *Evolutionary Algorithms for Solving Multi-Objective Problems*, 2nd edn. Springer, New York (2007)
12. De Maio, A., De Nicola, S., Huang, Y., Zhang, S., Farina, A.: Code design to optimize radar detection performance under accuracy and similarity constraints. *IEEE Trans. Signal Process.* **56**(11), 5618–5629 (2008)
13. De Maio, A., De Nicola, S., Huang, Y., Palomar, D.P., Zhang, S., Farina, A.: Code design for radar STAP via optimization theory. *IEEE Trans. Signal Process.* **58**(2), 679–694 (2010)
14. De Maio, A., Huang, Y., Piezzo, M., Zhang, S., Farina, A.: Design of optimized radar codes with a peak to average power ratio constraint. *IEEE Trans. Signal Process.* **59**(6), 2683–2697 (2011)
15. De Maio, A., Piezzo, M., Farina, A., Wicks, M.: Pareto-optimal radar waveform design. *IET Radar Sonar Navig.* **5**(4), 473–482 (2011)
16. De Maio, A., Piezzo, M., Iommelli, S., Farina, A.: Design of Pareto-optimal radar receive filters. *Int. J. Electron. Telecommun.* **57**(4), 477–481 (2011)
17. Deb, K.: *Multi-Objective Optimization Using Evolutionary Algorithms*, 1st edn. Wiley, New York (2001)
18. Deb, K., Pratap, A., Agarwal, S., Meyarivan, T.: A fast and elitist multiobjective genetic algorithm: NSGA-II. *IEEE Trans. Evol. Comput.* **6**(2), 182–197 (2002)
19. DeLong, D., Hofstetter, E.: On the design of optimum radar waveforms for clutter rejection. *IEEE Trans. Inf. Theory* **13**(3), 454–463 (1967)
20. Edgeworth, F.Y.: *Mathematical Physics: An Essay on the Application of Mathematics to the Moral Sciences*. C. K. Paul & Co., London (1881)
21. Enslin, J.W.: An evolutionary algorithm approach to simultaneous multi-mission radar waveform design. Master’s thesis, Rochester Institute of Technology, Rochester, NY (2007)
22. Garren, D.A., Odom, A.C., Osborn, M.K., Goldstein, J.S., Pillai, S.U., Guerci, J.R.: Full-polarization matched-illumination for target detection and identification. *IEEE Trans. Aerosp. Electron. Syst.* **38**(3), 824–837 (2002)
23. Gini, F., De Maio, A., Patton, L.K.: *Waveform design and diversity for advanced radar systems*. Inst of Engineering & Technology (2011)

24. Hurtado, M., Zhao, T., Nehorai, A.: Adaptive polarized waveform design for target tracking based on sequential Bayesian inference. *IEEE Trans. Signal Process.* **56**(3), 1120–1133 (2008)
25. Kay, S.: Optimal signal design for detection of Gaussian point targets in stationary Gaussian clutter/reverberation. *IEEE J. Sel. Top. Signal Process.* **1**(1), 31–41 (2007)
26. Kay, S.M.: *Fundamentals of Statistical Signal Processing: Estimation Theory*. Prentice Hall PTR, Upper Saddle River (1993)
27. Knott, E.F.: Radar cross section. In: Skolnik, M.I. (ed.) *Radar Handbook*, 2nd edn. McGraw-Hill, Inc., New York (1990). Chap. 11
28. Krolik, J.L., Farrell, J., Steinhardt, A.: Exploiting multipath propagation for GMTI in urban environments. In: *Proc. IEEE Radar Conf.*, pp. 65–68 (2006)
29. Leshem, A., Naparstek, O., Nehorai, A.: Information theoretic adaptive radar waveform design for multiple extended targets. *IEEE J. Sel. Top. Signal Process.* **1**(1), 42–55 (2007)
30. Li, J., Guerci, J.R., Xu, L.: Signal waveform's optimal-under-restriction design for active sensing. *IEEE Signal Process. Lett.* **13**(9), 565–568 (2006)
31. Li, J., Xu, L., Stoica, P., Forsythe, K.W., Bliss, D.W.: Range compression and waveform optimization for MIMO radar: a Cramér–Rao bound based study. *IEEE Trans. Signal Process.* **56**(1), 218–232 (2008)
32. Mahalanobis, P.C.: On the generalized distance in statistics. *Proc. Natl. Inst. Sci. India* **2**, 49–55 (1936)
33. Marler, R.T., Arora, J.S.: Survey of multi-objective optimization methods for engineering. *Struct. Multidiscip. Optim.* **26**(6), 369–395 (2004)
34. May, T., Rohling, H.: Orthogonal frequency division multiplexing. In: Molisch, A.F. (ed.) *Wideband Wireless Digital Communications*, pp. 17–25. Prentice Hall PTR, Upper Saddle River (2001)
35. Nehorai, A., Gini, F., Greco, M.S., Suppappola, A.P., Rangaswamy, M.: Introduction to the issue on adaptive waveform design for agile sensing and communication. *IEEE J. Sel. Top. Signal Process.* **1**(1), 2–5 (2007)
36. Pandharipande, A.: Principles of OFDM. *IEEE Potentials* **21**(2), 16–19 (2002)
37. Pareto, V.: *Cours D'Economie Politique*, vols. I and II. F. Rouge, Lausanne (1896)
38. Patton, L.K.: On the satisfaction of modulus and ambiguity function constraints in radar waveform optimization for detection. Ph.D. thesis, Wright State University, Dayton, OH (2009)
39. Patton, L.K., Rigling, B.D.: Modulus constraints in adaptive radar waveform design. In: *Proc. IEEE Radar Conf.*, Rome, Italy, pp. 1–6 (2008)
40. Patton, L.K., Rigling, B.D.: Autocorrelation and modulus constraints in radar waveform optimization. In: *Proc. Intl. Waveform Diversity & Design Conf.*, Kissimmee, FL, pp. 150–154 (2009)
41. Pillai, S.U., Oh, H.S., Youla, D.C., Guerci, J.R.: Optimal transmit-receiver design in the presence of signal-dependent interference and channel noise. *IEEE Trans. Inf. Theory* **46**(2), 577–584 (2000)
42. Rihaczek, A.W.: Optimum filters for signal detection in clutter. *IEEE Trans. Aerosp. Electron. Syst.* **AES-1**, 297–299 (1965)
43. Rummeler, W.D.: A technique for improving the clutter performance of coherent pulse train signals. *IEEE Trans. Aerosp. Electron. Syst.* **AES-3**(6), 898–906 (1967)
44. Sen, S., Nehorai, A.: OFDM MIMO radar with mutual-information waveform design for low-grazing angle tracking. *IEEE Trans. Signal Process.* **58**(6), 3152–3162 (2010)
45. Sen, S., Nehorai, A.: Adaptive OFDM radar for target detection in multipath scenarios. *IEEE Trans. Signal Process.* **59**(1), 78–90 (2011)
46. Sen, S., Hurtado, M., Nehorai, A.: Adaptive OFDM radar for detecting a moving target in urban scenarios. In: *Proc. Intl. Waveform Diversity & Design (WDD) Conf.*, Orlando, FL, pp. 268–272 (2009)
47. Sen, S., Tang, G., Nehorai, A.: Multi-objective optimized OFDM radar waveform for target detection in multipath scenarios. In: *44th Asilomar Conf. on Signals, Systems and Computers*, Pacific Grove, CA (2010)

48. Sen, S., Tang, G., Nehorai, A.: Multi-objective optimization of OFDM radar waveform for target detection. *IEEE Trans. Signal Process.* **59**(2), 639–652 (2011)
49. Sira, S.P., Papandreou-Suppappola, A., Morrell, D.: Dynamic configuration of time-varying waveforms for agile sensing and tracking in clutter. *IEEE Trans. Signal Process.* **55**(7), 3207–3217 (2007)
50. Skolnik, M.I.: *Introduction to Radar Systems*, 3rd edn. McGraw-Hill, New York (2002)
51. Spafford, L.: Optimum radar signal processing in clutter. *IEEE Trans. Inf. Theory* **14**(5), 734–743 (1968)
52. Tang, G., Nehorai, A.: Performance analysis of sparse recovery based on constrained minimal singular values. *IEEE Trans. Signal Process.* **59**(12), 5734–5745 (2011)
53. Van Trees, H.L.: Optimum signal design and processing for reverberation-limited environments. *IEEE Trans. Mil. Electron.* **9**(3), 212–229 (1965)
54. Weinmann, F.: Frequency dependent RCS of a generic airborne target. In: *URSI Int. Symp. Electromagnetic Theory (EMTS)*, Berlin, Germany, pp. 977–980 (2010)
55. Wicks, M.C.: A brief history of waveform diversity. In: *Proc. IEEE Radar Conf.*, Pasadena, CA, pp. 1–6 (2009)
56. Wicks, M.C., Mokole, E., Blunt, S., Schneible, R., Amuso, V. (eds.): *Principles of Waveform Diversity and Design*. SciTech Pub., Raleigh (2010)
57. Zitzler, E., Laumanns, M., Bleuler, S.: A tutorial on evolutionary multiobjective optimization. In: Gandibleux, X., Sevaux, M., Sörensen, K., T’kindt, V. (eds.) *Metaheuristics for Multiobjective Optimisation*. Springer Lecture Notes in Economics and Mathematical Systems, vol. 535, pp. 3–37. Springer, Berlin (2004)